The Astrophysical Journal, 961:32 (9pp), 2024 January 20 https://doi.org/10.3847/1538-4357/ad05c2

Exploring the Circumstellar Environment of Tycho's Supernova Remnant. I. The Hydrodynamic Evolution of the Shock

Ryosuke Kobashi[1], Shiu-Hang Lee[1,2], Takaaki Tanaka[3], and Keiichi Maeda[1]
[1] Department of Astronomy, Kyoto University, Kitashirakawa, Oiwake-cho, Sakyo-ku, Kyoto 606-8502, Japan; kobashi@kusastro.kyoto-u.ac.jp
[2] Kavli Institute for the Physics and Mathematics of the Universe (WPI), The University of Tokyo, Kashiwa 277-8583, Japan
[3] Department of Physics, Konan University, 8-9-1 Okamoto, Higashinada, Kobe, Hyogo 658-8501, Japan
Received 2023 May 31; revised 2023 October 10; accepted 2023 October 21; published 2024 January 11

Abstract

Among Type Ia supernova remnants (SNRs), Tycho's SNR has been considered as a typical object from the viewpoints of its spectroscopic, morphological, and environmental properties. A recent reanalysis of Chandra data showed that its forward shock is experiencing a substantial deceleration since around 2007, which suggests recent shock interactions with a dense medium as a consequence of a cavity-wall environment inside a molecular cloud. Such a nonuniform environment can be linked back to the nature and activities of its progenitor. In this study, we perform hydrodynamic simulations to characterize Tycho's cavity-wall environment using the latest multiepoch proper motion measurements of the forward shock. A range of parameters for the environment is explored in the hydrodynamic models to fit with the observational data for each azimuthal region. Our results show that a wind-like cavity with $\rho(r) \propto r^{-2}$ reconciles with the latest data better than a uniform medium with a constant density. In addition, our best-fit model favors an anisotropic wind with an azimuthally varying wind parameter. The overall result indicates a mass-loss rate which is unusually high for the conventional single-degenerate explosion scenario.

Unified Astronomy Thesaurus concepts: Proper motions (1295); Molecular clouds (1072); Circumstellar matter (241); X-ray sources (1822); Supernova remnants (1667); Type Ia supernovae (1728)

1. Introduction

Despite an incomplete understanding of their progenitor systems and populations, Type Ia supernovae (SNe Ia) originating from the thermonuclear explosions of white dwarfs in binary systems have been used as a standard candle for cosmological studies (Riess et al. 1998; Perlmutter et al. 1999). The nature of the progenitor system of SNe Ia is a matter of hot debate, which is now mainly split into two camps of scenarios depending on whether the companion star is another white dwarf or a nondegenerate star, which are nowadays referred to as the double degenerate (DD) and single degenerate (SD) scenarios, respectively.

Tycho's supernova remnant (Tycho's SNR; SN 1572, G120.1+1.4; hereafter Tycho) is considered to originate in a normal SN Ia explosion that happened in 1572 November. A wealth of observations have been made, such as spectroscopic observations and modeling of the thermal X-ray emission from the ejecta (e.g., Badenes et al. 2006; Yamaguchi et al. 2014, 2017), the circumstellar environment and morphology (Reynoso et al. 1997; Hwang et al. 2002; Kothes et al. 2006; Williams et al. 2013; Lopez et al. 2015), attempts of searching for the companion donor star (Ruiz-Lapuente et al. 2004; Kerzendorf et al. 2009; Xue & Schaefer 2015), the nondetection of a Strömgren sphere (Rappaport et al. 1994; Ghavamian et al. 2003; Woods et al. 2017), and light echoes (Krause et al. 2008). However, no consensus has been reached so far as for whether the SNR originates from the DD or SD channel, with competing evidence from both camps.

Tycho has recently been considered to be surrounded by an azimuthally nonuniform preshock density environment; Katsuda et al. (2010) measured the proper motion of the forward shock (FS) at different azimuthal regions, and Williams et al. (2016) found an offset of the explosion center from the geometric center. It has been suggested that the progenitor of Tycho is further surrounded by a wind-like environment with a molecular cloud, which has led Zhou et al. (2016) to propose the SD scenario. However, the issue has been controversial, with a counterargument (pointing to nonassociation with the molecular cloud) presented by Woods et al. (2017), who favored the DD scenario. This was recently settled by recent work by Tanaka et al. (2021; hereafter T+21), who examined the long-term time evolution of the shock expansion through a proper motion study using Chandra archival data; they revealed a substantial deceleration of the shock in the last couple decades, probably caused by the existence of an outer dense region of circumstellar matter (CSM), e.g., molecular clouds. Such a wind-like bubble adds another source of credibility to the SD scenario for the case of Tycho. Similar expanding bubble shells have also been discovered in other Galactic and extragalactic SNRs (Sano et al. 2022; Guest et al. 2023).

In this work, we utilize the new proper motion results in an attempt to refine the picture of the environment surrounding this important historic SNR. First, we constrain the distance and cavity density of Tycho by using FS and reverse shock (RS) observations simultaneously (Warren et al. 2005; Yamaguchi et al. 2014). For a given cavity density (and the corresponding distance), we calculate the shock dynamics using hydrodynamics simulations, search for the best-fit environmental parameters, and then compare them with the evolution of the shock radius observed by T+21 using a goodness-of-fit parameter (χ^2). A few scenarios for the circumstellar environment are explored and their compatibility with the latest proper motion data are assessed. We focus primarily on the environmental aspects in this study and use

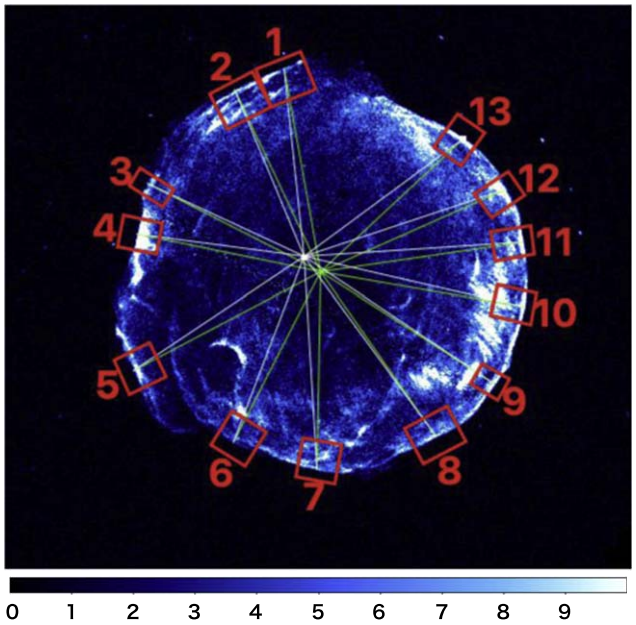

Figure 1. Chandra ACIS image of Tycho's SNR in 2009 (reproduced from T+21's data). The color bar shows the flux from each pixel in units of 10^{-9} photon cm^{-2} s^{-1}. The red rectangles are the regions we use. Green or white lines indicate the line segment connecting the FS in each azimuthal angle with the geometric center or pressure center, respectively.

fixed parameters for the SN explosion itself, which will be discussed in more details in a follow-up work.

In Section 2, we define models for the environment and introduce our numerical method. In Section 3, we explore models with a uniform cavity for the environment and demonstrate the difficulty of reproducing the latest proper motion data in these kinds of environments. In Section 4, we switch to the case of a wind-like cavity and search for the best-fit parameters, such as the pre-SN mass-loss rates and gas cloud densities. Section 5 is devoted to a discussion of how our best-fit models stand in the existing scenarios of Type Ia SNR progenitors. Section 6 concludes our work.

2. Setup and Models

The observational data of the proper motion of the FS (T+21; in the synchrotron-dominated X-ray band) are split into four epochs of 2003, 2007, 2009, and 2015. We use the data from 2003 as an anchor and define positional shifts using the 2003 data as a reference point. To this end, we assume two possible locations for the explosion center, i.e., the geometric center from Warren et al. (2005; consistent with the one estimated from the 3D proper motion of the ejecta in Millard et al. 2022; Godinaud et al. 2023) and the one derived in Williams et al. (2016) where a global pressure gradient is assumed (hereafter "pressure center"). The data from each epoch are divided into 13 azimuthal regions in a counter-clockwise order from the north, i.e., Regions 1–13, as shown in Figure 1.[4]

We consider two categories for the cavity-wall models (see the top panel of Figure 2), i.e., an inner bubble with a uniform density ρ_0, and one with a wind-like profile with density $\rho(r) = ar^{-2}$, each surrounded by a dense outer region. The cavity-wall structure is supposed to be the result of pre-SN progenitor activity interacting with a surrounding molecular cloud (T+21). The shock is fast when it is propagating inside the inner low-density bubble. As it starts penetrating into the dense region at a certain radius, a rapid deceleration of the shock as seen in T+21 is expected. According to upper panel of Figure 2 in T+21 Regions 5–8 can be used for calibration of our models as the shocks in these portions most likely have not yet started interacting with the dense cloud by 2003 and are still inside the cavity, meaning that only one parameter is involved (i.e., the inner cavity density). Thus, in Sections 3.1 and 4.1, we use the 2003 and 2007 data in Regions 7 and 8 (we omit Regions 5 and 6, where there is no measurement for the RS radius) for constraining Tycho's distance as a function of the cavity density. After determining the distance, we move on to the models with an outer dense cloud with a density $\rho_{\rm mc}$, which will be discussed in Sections 3.2 and 4.2. The bottom panel of Figure 2 shows the impact of each of the parameters on the density profile of our CSM model. The radial boundary of the cavity (or inner cloud radius) is $r = R_{\rm c}$, and the transition length between the cavity and cloud is characterized by the parameter Δr. The CSM is assumed to have, from inside to outside, a low-density cavity within $r < R_{\rm c}$, a density gradient connecting the cavity and cloud at a radius $R_{\rm c} < r < R_{\rm c} + \Delta r$, and a dense cloud at $r > R_{\rm c} + \Delta r$. For simplicity, we consider 3×3 patterns of ($\rho_{\rm mc}$, Δr), with $\rho_{\rm mc} \in [10^{-23}, 10^{-22}, 10^{-21}]$ g cm^{-3} and $\Delta r \in [0.04, 0.4, 1.0]$ pc. We also do not consider episodic mass loss, which is reserved for future work in which hydrodynamic models of wind-blown bubbles will be discussed.

For the ejecta, we use a single canonical thermonuclear explosion model with a near-Chandrasekhar mass white dwarf, i.e., an ejecta mass of 1.4 $M_\odot$, an explosion kinetic energy of 1.0×10^{51} erg, and an exponential density profile for the initial ejecta (Dwarkadas & Chevalier 1998).

The time evolution in our models is followed by the 1D spherically symmetric hydrodynamic code[5] *VH-1* (Blondin & Ellison 2001) on a Lagrangian grid, in which radiative cooling is accounted for using a cooling curve from Sutherland & Dopita (1993; see Kobashi et al. 2022).

3. Uniform-cavity Models

3.1. Calibration of Cavity Parameters and Estimates of the Distance

We first consider a uniform ambient environment with a constant density $\rho_{\rm c}$ ignoring the effect of an outer dense region, and focus on the relation between $\rho_{\rm c}$ and the distance D of Tycho from Earth. Despite the many works done so far (see Hayato et al. 2010, Figure 6), there still remain large uncertainties among the literature values on the distance to Tycho. A precise knowledge of the distance is especially crucial to break degeneracy during comparison between the observational data (in angular scale) and hydrodynamic models (in physical scale). From the observed angular radius θ of the FS using the synchrotron-dominated X-ray emission (T+21), we can calculate the distance as $R_{\rm sim}(\rho_{\rm c})/\theta$ from the model radius $R_{\rm sim}(\rho_{\rm c})$ assuming a certain value for the density of the

[4] We use the same "position number" as in T+21 for the regions.

[5] By treating each azimuthal region using independent 1D hydrodynamic models, we are ignoring additional multidimensional effects such as possible clumpiness in the environment and an asymmetric thermonuclear explosion (see, e.g., Millard et al. 2022). The discussion of these effects is postponed to a follow-up work currently in progress using results from fully 3D hydrodynamic models.

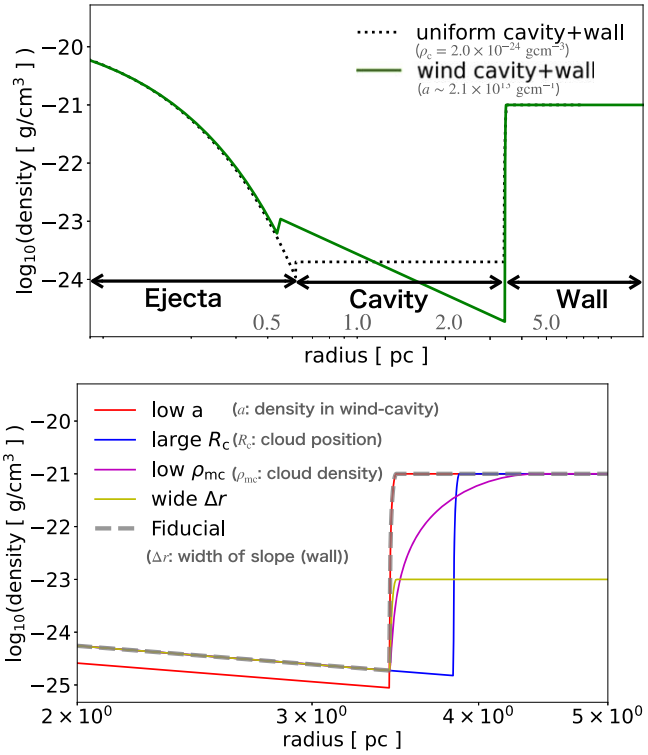

Figure 2. Upper panel: the initial density profile of the two model categories: one for the uniform-density cavity case (black line; with $\rho_c = 2.0 \times 10^{-24}$ g cm^{-3}), and the other for the wind-like cavity case (green line; with $a = 2.1 \times 10^{13}$ g cm^{-1}, which corresponds to $\dot{M} = 1.047 \times 10^{-4}\ M_\odot$ yr^{-1} for $V_w = 250$ km s^{-1}). Lower panel: the initial density profiles of the wind-like cavity model, showing the effect of varying different parameters: the density in the wind cavity a (red), the cloud position R_c (blue), cloud density ρ_{mc} (yellow), and the gap between cavity and cloud Δr (magenta). The fiducial model is shown by the gray dashed line.

ambient medium. Furthermore, we can further narrow down the value by performing a similar calculation for the RS.

Likewise, there exists uncertainty in the density estimations (see T+21 and references therein). For the angular radii θ of the FS and RS at each region, we use the observational results from Warren et al. (2005) as a reference. For simplicity, we use the Kα peak as in Warren et al. (2005) for pinning down the RS position, although we are aware that there is evidence for some regions that the RS radius can be smaller if the Fe-Kβ peak is used as a beacon for the RS location instead of Kα by considering the postshock ionization length scale (e.g., Yamaguchi et al. 2014). The analysis of the Fe-Kβ peak, however, has been performed only for the northwest region, and such analyses for other azimuthal regions are not yet available. We anticipate that an extension to the usage of Fe-Kβ data can be done consistently when an observation along the full azimuthal circle will be performed in the future.

In Figure 3, we plot the density–distance relations by using the FS and RS measurements from 2003 to constrain Regions 7 and 8 (in which the SNR has presumably started interacting with the dense region well after 2003; see Section 2). The overlapping regimes in the ρ_c–D parameter space, i.e., where the blue lines overlap with the red shaded area, show the allowed ranges, being consistent with both the FS and RS data simultaneously. We hence obtain the estimates of D and ρ_c as $\sim$3 kpc and $\sim 2 \times 10^{-24}$ g cm^{-3}, respectively. The results are shown under two assumptions on the explosion center location as well, as discussed above.

3.2. Proper Motion Simulation

Using the relation obtained in Section 3.1, here we perform hydrodynamic simulations with different environment models and compare them with the data for the FS position to assess their compatibility with the observations.

Figure 4 shows the model evolution of the FS radius for an environment with a constant density ρ_c. Here, without the complexity from cloud interaction, we can first compare a model consistent with the ρ_c–D relation obtained above (red line) with the 2003–2015 data. The model clearly underpredicts the angular size of Tycho in the 2007 to 2015 data. An ad hoc attempt to realize a faster expansion by using a smaller ambient density (black, gray, and blue lines) fails to account for this discrepancy, since the larger shock velocity in a more tenuous medium is offset by a larger required distance as shown in Figure 3, so that the apparent angular velocity (or size) is only moderately affected as we can see in Figure 4. Instead, when a wind-like cavity is incorporated (dashed green line, see Section 4 for details), the $\rho \propto r^{-2}$ density structure in the ambient environment helps realize an overall faster angular expansion to reconcile better with the observed size at each epoch, giving support to a wind-like environment around Tycho in its earlier evolution stage before its blastwave hits the dense wall. This result from fitting to data in Regions 7 and 8 provides a motivation to explore wind-like models for the environment of Tycho, and study their implications on its progenitor system in the next sections.

4. Wind-cavity Models

The existence of a progenitor wind for a Type Ia SNR is supported by some previous studies (see Section 1). The failure of the models with a uniform cavity to explain the time evolution of the proper motion of Tycho as we have seen above leads us to explore models invoking a pre-SN wind-blown bubble. We will separate the discussion into isotropic wind and anisotropic wind cases.

4.1. Calibration of the Cavity Parameters and Distance Estimations

For the wind-cavity models, we follow similar steps as above but now with wind parameter $a \equiv \dot{M}/(4\pi V_w)$ instead of ρ_c, where $\dot{M}$ is the mass-loss rate that is scaled by the reference wind velocity (V_w), taken as 250 km s^{-1} according to Zhou et al. (2016). From the FS and RS data in Regions 7 and 8 again, we obtain results on the a versus D plane (Figures 5(a) and (b)) and thus constrain D. A unique range of D is determined from the simultaneous fit to both regions (see the magenta band in Figure 5(c)). This estimate of D ranges over a narrow window of 3.37–3.64 kpc (3.52–3.78 kpc if the pressure center is assumed). Hereafter, we will use the median of this range as our estimate of D for the analysis in all regions, which is reasonable given the small allowed range.

Using the obtained estimate of D, the appropriate wind parameter $a = a_{\rm region}$ in other regions can be estimated (Figure 5(d)) using the relation $R_{\rm sim,FS}(a_{\rm region}) = D\theta_{\rm region}$. These values are obtained under the assumption that the FS has not hit the dense cloud before the 2003 epoch in all regions, which is not guaranteed to be true. As a result, these $a_{\rm region}$ ($a \sim$ a few 10^{13} g cm^{-1}; $\dot{M} \sim 10^{-4}\ M_\odot$ yr^{-1}, and $V_w = 250$ km s^{-1}) values serve only as rough order estimates. We can see that the resulting wind parameter $a_{\rm region}$ is around 100 times larger than that

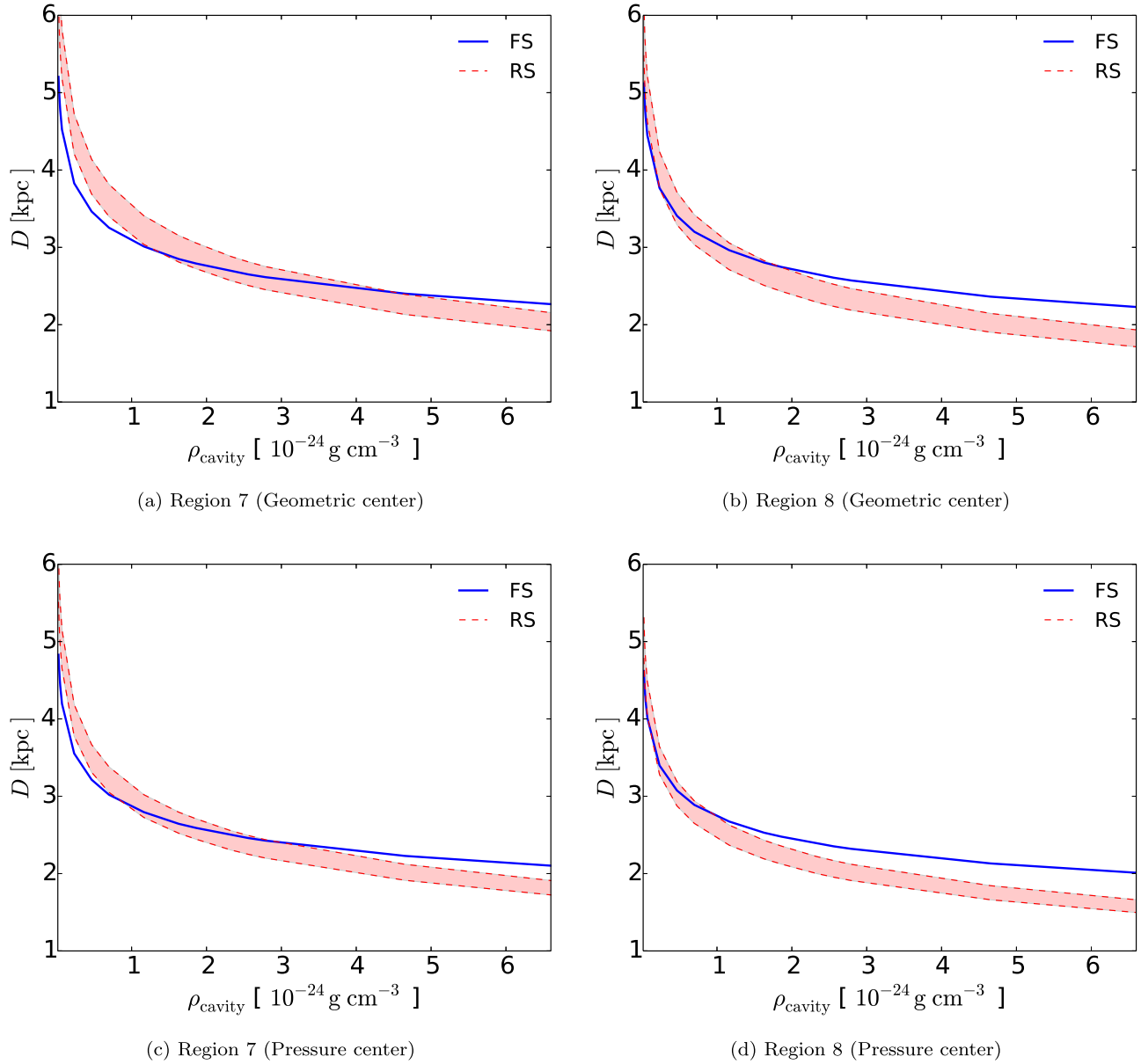

(a) Region 7 (Geometric center)

(b) Region 8 (Geometric center)

(c) Region 7 (Pressure center)

(d) Region 8 (Pressure center)

Figure 3. Cavity density vs. distance results from our hydrodynamic models constrained by the FS (blue lines) and RS (red regions) observational data. The ranges where the blue lines overlap with the red shaded area are consistent with both the FS and RS data simultaneously. The left and right panels respectively correspond to the results from Region 7 and Region 8, where the geometric (pressure gradient) explosion center is assumed in the upper (bottom) panels.

predicted for a normal accretion wind from the well-known Hachisu model (see Section 5.1 for the discussion on order estimate).

4.2. Proper Motion Simulation

Likewise to Section 3.2, we perform hydrodynamic simulations under various environment parameters to compare with the proper motion data using the distance D obtained in Section 4.1. This time, we will investigate isotropic wind (Section 4.2.1) and anisotropic wind cases (Section 4.2.2) in the following.

To compare the model angular radius with the data quantitatively, we use χ^2 for the goodness-of-fit, i.e.,

$$\chi^2 = \sum_{i=1}^{4} \frac{(y_i - m_i)^2}{\sigma^2}, \quad (1)$$

where $i = 1$, 2, 3, and 4 correspond to the 2003, 2007, 2009, and 2015 epochs, respectively, y_i are the observed values, and m_i are the values from our model, and σ is the rough "average error" to make χ^2 a reasonable value by $\sigma = (\alpha_1 + \alpha_2 + \alpha_3)/3$ where α_i is the error accompanied with the data of positional shifts $(y_i - y_1)$.

4.2.1. Case with an Isotropic Wind

In this set of models, we fix the wind parameter a to a unique and common value for all azimuthal angles. The FS angular radii over the azimuthal circle measured in the 2003 epoch are found to vary from $\sim$200″ to $\sim$260″, and the maximum radius is recorded at Region 5. As a test, we pick the wind parameter obtained for Region 5, i.e., $a = a_{\mathrm{region,5}}$, and apply it to the other regions to see if satisfactory fits can be obtained with a

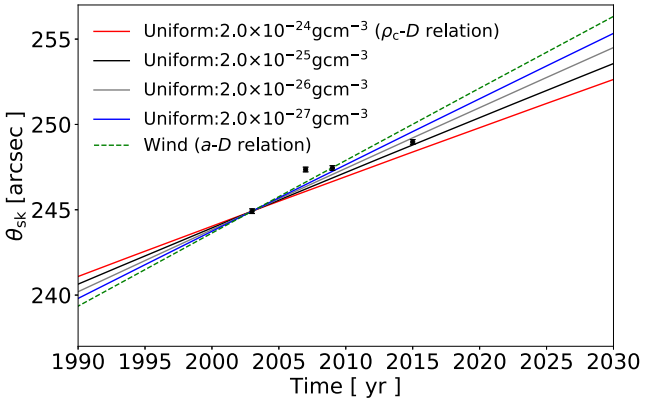

Figure 4. Time evolution of the FS radius for the case of a uniform cavity compared with data in Region 7, with the geometric explosion center is assumed. The red line shows a model with parameters consistent with both the FS and RS radii at 2003. The others assume smaller cavity densities with corresponding distances. A wind-like model is also shown with the green dotted line. The choice of explosion center is not critical to the result, and a similar result is obtained for Region 8.

variable cloud parameter. The fitting in the other regions turns out to be difficult using the wind model best fitted for Region 5, mainly because the slope between the 2003–2007 epochs is so steep that even models with the FS interacting with the dense cloud from well before 2003 cannot explain the data. An example for Region 9 is shown in Figure 6(b). Obviously, a single set of wind parameter (isotropic wind) for Tycho's surrounding falls short of being able to explain the overall dynamics of the shock around the azimuth. Therefore, we next propose another set of models with an anisotropic wind, which use a variable wind parameter as a function of θ, to see if we can get an improvement to the fits.

4.2.2. Case with an Anisotropic Wind

A similar methodology as in Section 4.2.1 is applied for the anisotropic wind case but now with the wind parameters treated independently for the different regions. As shown in Figure 7, the data for Region 9 can now be well fitted this time using an anisotropic wind model.

During the parameter survey, we explore 3×3 patterns for the cloud density $\rho_{\rm mc}$ and the transition length Δr for each combination of cloud position $R_{\rm c}$ and wind parameter a. We pick the best-fit parameter set ($\rho_{\rm mc}$, Δr) with the minimum χ^2 out of those 3×3 models, and repeat the survey on the wind parameter a (except for Regions 7 and 8 for which we can use the fixed $a = a_{\rm region}$ for the reasons discussed above), and $R_{\rm c}$. The results for the best-fit parameter sets in all regions are summarized in Table 1. The results of χ^2 over the explored parameter space are shown in Figure 8 for Regions 1 and 6 as an example, from which we can see that an effective constraint can be obtained, where the distance D is assumed to be ~ 3.5 kpc (~ 3.7 kpc if the pressure center is assumed) within the range estimated in Section 4.1.

4.3. Emerging Picture of Tycho's CSM

Using the χ^2 values, we find that the best-fit $R_{\rm c}$ can either be smaller than R_{2003} or between R_{2003} and R_{2015} depending on the regions, as shown in Figure 9(a). This trend shows that the shock in some regions had already started experiencing cloud interaction before 2003, and the shock front in the other regions has started penetrating into the dense wall between 2003 and 2015. Indeed, Hα filaments have been observed in some regions especially in the east (Lee et al. 2010), which can result from shock–cloud interaction that started earlier than in the other regions. In any case, we find that the FS of Tycho has been propagating in a tenuous wind bubble until only very recently for all azimuthal regions, meaning that the shape of the wind bubble can be well approximated by the current FS position. This makes the discrimination between models with different assumed explosion centers difficult from the point of view of FS dynamics. On the other hand, the wind density a has an approximate anticorrelation with R_{2003} and R_{2015}, and thus $R_{\rm c}$, but this may be attributed to our procedure determining D and a from R_{2003} and R_{2015}, which may not be consistent with a real trend.

Also, as shown in Figure 9(b), our best-fit model in each region predicts a steep density gradient from the large gap between $\rho(R_{\rm c})$ and $\rho_{2015} \equiv \rho(R_{\rm c}) + (R_{2015} - R_{\rm c})\frac{\partial \rho}{\partial r}$, where $\rho(R_{\rm c})$ is the gas density at the outer boundary of the wind cavity and ρ_{2015} is the density of the cloud that the shock is interacting within 2015, respectively. This density structure, which steeply increases outward, does imply an origin of the dense structure from a wind shell swept by a progenitor wind as suggested by Zhou et al. (2016) and T+21 before. The bumpy variation of ρ_{2015} over the azimuth is inconsistent with a more-or-less isotropic and uniform dense medium, but is attributable to the clumpiness of the surrounding cloud.

5. Discussion

5.1. On the Inferred Wind Properties

From our calculations above, we have obtained of order estimates for the wind properties in the cavity surrounding Tycho, with $a \sim 2 \times 10^{13}$ g cm^{-1} where $\rho(r) = ar^{-2}$ is assumed. The total mass in the free-expanding wind zone can then be expressed in polar coordinates (r, ψ, ϕ),

$$\begin{aligned} M_{\rm wind} &= \int_0^{R_{\rm c,Region}} r^2 dr \int_{-1}^{1} d(\cos(\psi - \delta\psi)) \int_0^{2\pi} d\phi \; ar^{-2} \\ &\sim 1.665 \pm 0.055 \, M_\odot (1.46 \pm 0.2 \, M_\odot; \text{ pressure center}), \end{aligned} \quad (2)$$

where ψ is the azimuthal angle and ϕ is the polar angle. Here we have assumed that the wind is symmetric over ϕ such that the sky-projected wind bubble is symmetric along $\psi = \delta\psi$. For $\delta\psi$, we use $\delta\psi = 78.^\circ4$ and $260.^\circ3$, roughly corresponding to Region 3 and Region 10 where the maximum and minimum of $aR_{\rm c,Region}$ are located, respectively. The estimated $M_{\rm wind}$ suggests that the pre-SN mass loss is about one to a few solar masses.[6] The derived CSM mass far exceeds the mass budget available in the DD scenario. On the other hand, this is consistent with the SD scenario, where the mass budget for the CSM can be attributed to the companion star whose initial mass is $\sim$2–4 $M_\odot$ (Hachisu et al. 1999). It is difficult to use the DD scenario to explain this CSM property because such a large mass loss can hardly occur during its pre-SN activities.

[6] We note that this estimate can vary to some extent if the Fe-Kβ emission is used as a proxy of the location of the RS instead of Kα, as we have mentioned above.

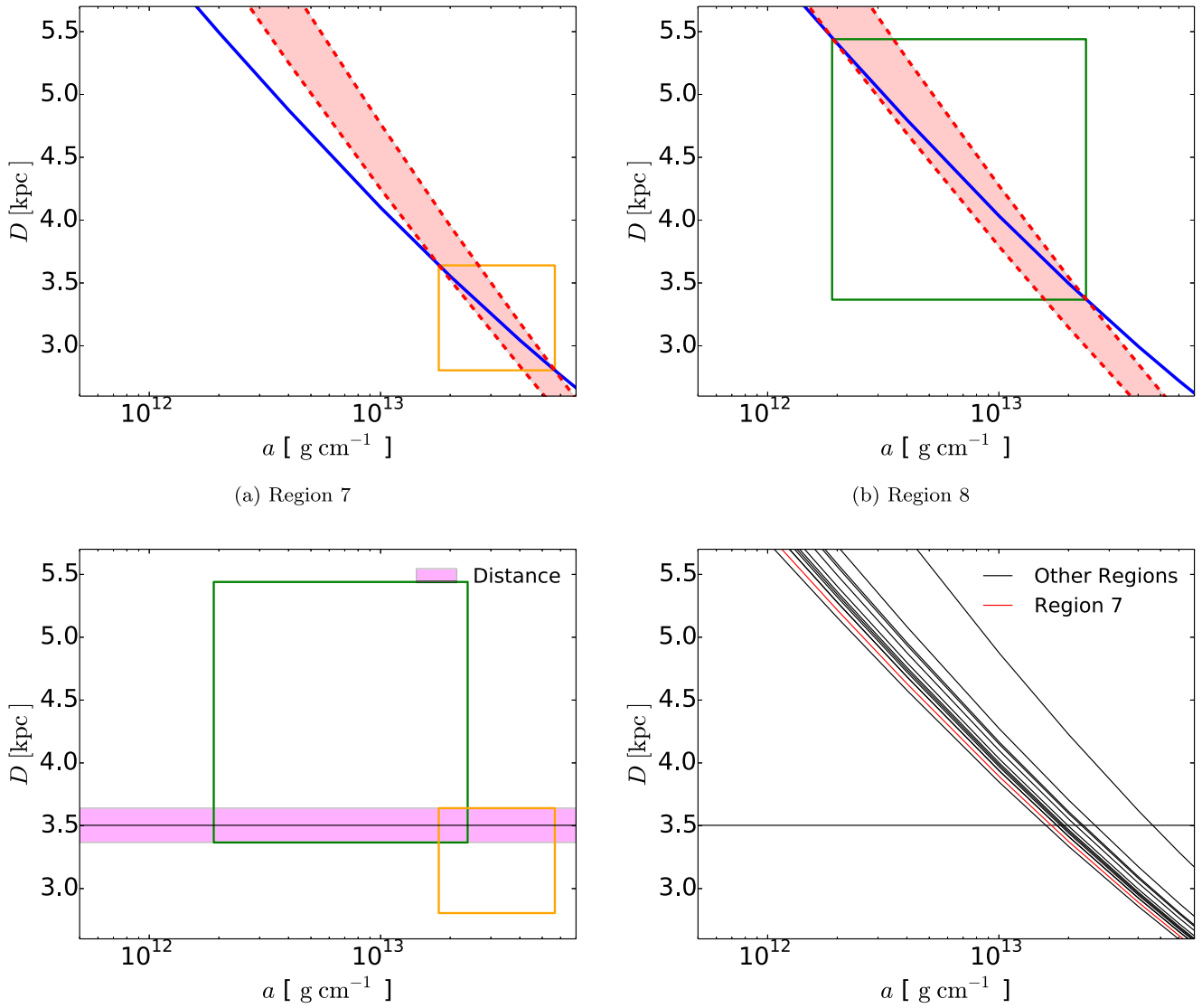

(a) Region 7

(b) Region 8

(c) Combined constraints on D

(d) Rough estimates of a in all regions

Figure 5. Panels (a) and (b): wind parameter a vs. distance from our hydrodynamic models constrained by the FS (blue lines) and RS (red regions) data for Region 7 (a) and Region 8 (b). The orange and green boxes indicate the parameter range where the model is consistent with both the FS and RS data in Regions 7 and 8, with the overall constraint on a and D shown in panel (c). Panel (d): rough estimates for a in each region obtained by comparing the hydrodynamic models with the FS radii at the 2003 epoch in each region, but without accounting for any cloud interaction. The horizontal line is the median of the best-fit distance D from panel (c). The geometric explosion center is assumed for all results shown here.

The mass-loss rate could however place stronger constraints on the underlying scenarios, even for the SD scenario. With $V_{\rm w} = 250$ km s^{-1}, the pre-SN activity must have operated in the final $\sim$10,000 yr with a mass-loss rate of $\sim 10^{-4}\,M_\odot$ yr^{-1}. However, the mass-accretion rate onto the progenitor WD is believed to be limited to $<10^{-6}\,M_\odot$ in the canonical SD scenario toward a near-Chandrasekhar white dwarf (Nomoto 1984). Therefore, only $\sim$0.01 $M_\odot$ of mass was accumulated during this final phase, which unlikely leads to the formation of a near-Chandrasekhar white dwarf. This may be remedied if $V_{\rm w}$ is lower, e.g., $\sim$25 km s^{-1}, for which the mass accretion can exceed $\sim$0.1 $M_\odot$; it will probably require a slow wind associated with an extended donor, rather than the white dwarf wind. In this case, the extended envelope might have been stripped away by SN shock interaction (e.g., Marietta et al. 2000; Pakmor et al. 2008; Liu et al. 2012; Pan et al. 2012), and thus may leave only a very faint surviving companion which might be consistent with the nondetection of a surviving companion star (Ruiz-Lapuente et al. 2004; Kerzendorf et al. 2009; Xue & Schaefer 2015). The above constraint could also be overcome in the double-detonation scenario, i.e., an explosion initiated by runaway triple-alpha reactions on the accumulated He layer of the progenitor white dwarf (Nomoto 1982; Livne 1990; Shen & Bildsten 2009)—this scenario does not require a substantial increase of the white dwarf mass toward the explosion.

In view of the combination of the large mass budget and the high accretion rate, another appealing scenario is the core-degenerate scenario and its variants (e.g., Sparks & Stecher 1974; Soker 2015; Meng & Podsiadlowski 2017; Cui et al. 2022). This scenario may explain the large CSM mass by a common envelope interaction, and the ignition of the thermonuclear runaway by a rapid He accretion during the core merger of a white dwarf and He-rich companion (e.g., Jerkstrand et al. 2020). We however note

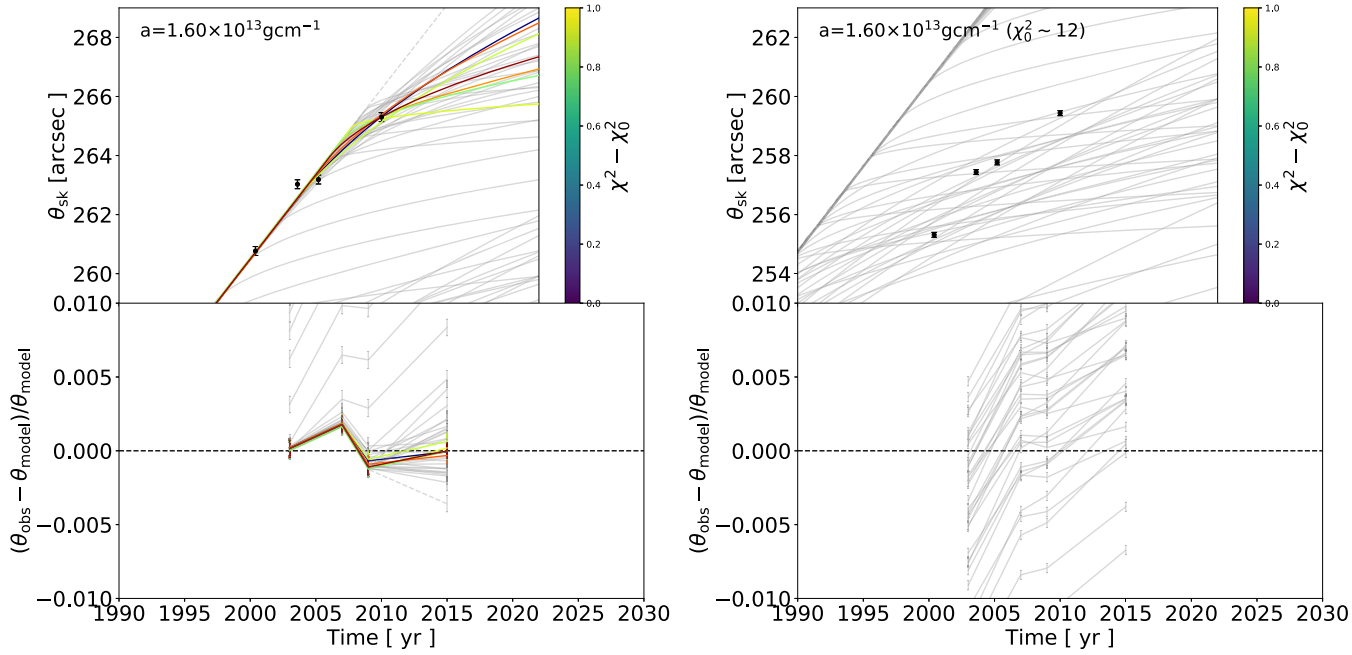

(a) Region 5 (b) Region 9

Figure 6. Time evolution of the FS radius assuming an isotropic wind-like environment in Regions 5 (panel (a)) and 9 (panel (b)). The lines are colored according to the color map if $\chi^2 \lesssim \chi_0^2 + 1$, or in gray otherwise, and χ_0^2 is the minimum χ^2 obtained. Note that here we use the χ_0^2 value obtained for Region 5 for the color bars in both panels, i.e., ∼12.2 in both panels ($\chi_0^2 \sim 175$ in Region 9) for the purpose of comparison. The geometric explosion center is assumed for all results shown here.

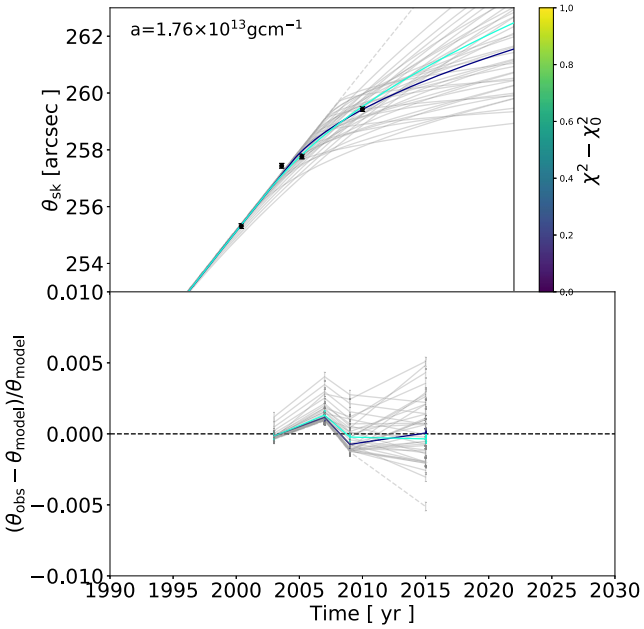

Figure 7. Same as Figure 6(b) but for the case of an anisotropic wind. The color bar is identical to that in Figure 6(b) but now scaled with $\chi_0^2 \sim 18.3$ for Region 9.

that such a scenario has not been investigated in detail (not to the level the SD and DD scenarios have been investigated), and thus its applicability to Tycho is still quite speculative.

5.2. Comparison with Previous Studies

5.2.1. The Size of the Wind Bubble

There are previous theoretical studies which considered wind-like environment models. This model is designed to reproduce the dense shocked ejecta shell required by the observed high ionization degree (Badenes et al. 2006) in the inner region, and the low density suggested from the expansion parameter (Reynoso et al. 1997; Katsuda et al. 2010) simultaneously. One such study, Chiotellis et al. (2013; see also Slane et al. 2014), used a more compact wind bubble smaller than 1.8 pc, which is less extended than in the model in the present study.

Now that Zhou et al. (2016) have shown that the shock is interacting with a dense gas shell, and T+21 and a recent Doppler motion analysis (Kasuga 2021) have suggested that shock–cloud interaction began around 2007 on average, a more consistent picture seems to point to a wind-shell radius nearly equal to the current shock radius, as suggested by the present work. The r^{-2} density profile assumed in this work in the wind cavity extending up to nearly the current FS radius can explain the dense shocked ejecta and a low-density surrounding environment ($\sim 10^{-25}$ g cm^{-3} at a radius of ∼3 pc) to reconcile with the observations.

5.2.2. Anisotropic Wind or Ejecta?

Millard et al. (2022) explained the azimuthal variation of the shock evolution using the azimuthal variation of the explosion properties by putting a larger kinetic energy into certain angles, e.g., the southeast region. While this time we have attributed the azimuthal variation of the shock proper motion mainly to the azimuthal variation of the wind density and the radial position of the dense cloud, a combined effect with an asymmetric explosion remains possible. However, recent 3D hydrodynamic simulations of Type Ia SNRs like Tycho from the SN phase have indicated that the SNR morphology will lose memory of its original asymmetric SN properties within a timescale of ∼100 yr after explosion (e.g., Ferrand et al. 2019).

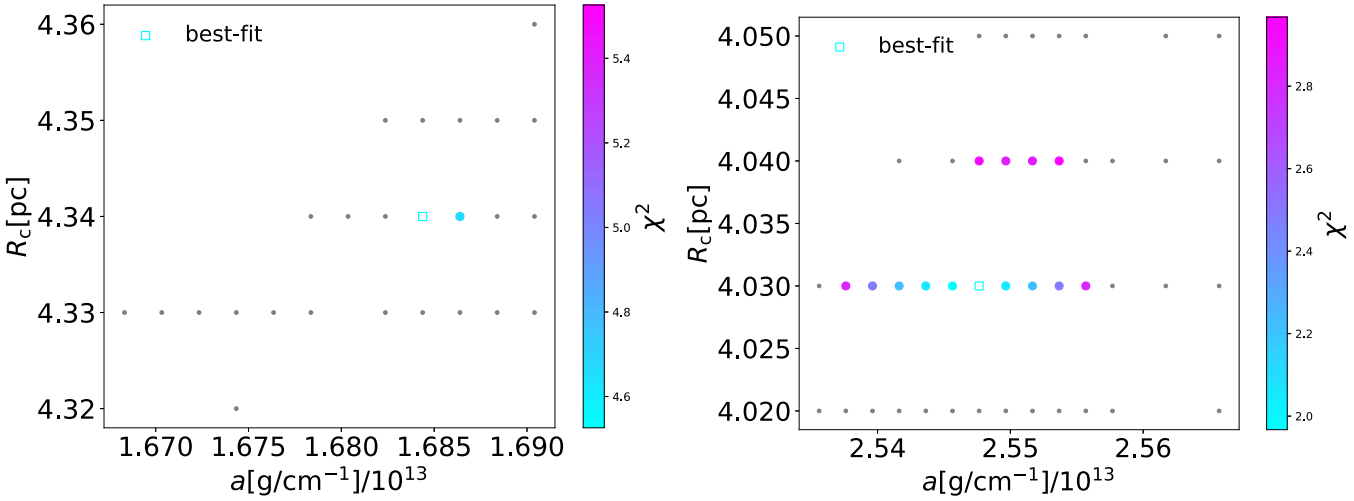

(a) Region 1 (b) Region 6

Figure 8. The χ^2 value corresponding to each parameter set of (a, R_c) when fixing (ρ_{mc}, Δr) to their corresponding best-fit values. Models satisfying the criterion $\chi^2 \leqslant \chi_0^2 + 1$ are shown by large points colored according to their χ^2 value, whereas an open square is used for the best-fit model with $\chi^2 = \chi_0^2$. The small gray points are for models with $\chi^2 > \chi_0 + 1$. The results for Region 1 (a) and Region 6 (b) are shown as examples. The geometric explosion center is assumed for the results shown here.

Table 1
Best-fit Model Parameters per Azimuthal Region

Region[a]	1	2	3	4	5	6	7	8	9	10	11	12	13
Panel A: Geometric Center													
$\dot{M}$ [10^{-4} $M_\odot$ yr^{-1}][b]	0.839	0.950	1.154	1.413	0.792	1.269	1.066	0.993	0.877	0.880	0.916	0.611	1.131
a [10^{13} g cm^{-1}][b]	1.68	1.91	2.32	2.84	1.59	2.55	2.14	1.99	1.76	1.77	1.84	1.89	2.27
R_c [pc][c]	4.34	4.19	4.08	3.91	4.44	4.03	4.21	4.29	4.35	4.29	4.26	4.21	4.02
$\frac{\partial\rho}{\partial r}$ [10^{-23} g cm^{-3} pc^{-1}][d]	2.48	0.99	100	25	2.5	25	250	2500	10	0.99	0.99	0.99	0.99
$R_{2015} - R_c$ [pc][e]	0.098	0.14	0.055	0.050	0.070	0.031	0.030	0.012	0.051	0.11	0.11	0.14	0.13
ρ_{2015} [10^{-24} g cm^{-3}][f]	2.54	1.55	54.8	12.9	1.82	7.78	51.0	297	5.16	1.17	1.15	1.41	1.60
Panel B: Pressure Center													
$\dot{M}$[10^{-4} $M_\odot$ yr^{-1}][b]	1.043	1.293	1.634	1.919	0.756	0.883	0.611	0.492	0.431	0.466	0.534	0.611	0.871
a [10^{13} g cm^{-1}][b]	2.09	2.60	3.28	3.85	1.52	1.77	1.23	0.988	0.865	0.936	1.07	1.23	1.75
R_c [pc][c]	4.14	3.94	3.77	3.66	4.50	4.38	4.74	4.94	5.02	4.95	4.78	4.62	4.27
$\frac{\partial\rho}{\partial r}$ [10^{-23} g cm^{-3} pc^{-1}][d]	2.5	0.98	100	100	10	250	2500	250	25	250	1.0	100	0.99
$R_{2015} - R_c$ [pc][e]	0.094	0.11	0.60	0.041	0.057	0.0098	0.0035	0.020	0.061	0.063	0.11	0.12	0.13
ρ_{2015} [10^{-24} g cm^{-3}][f]	2.44	1.26	59.9	41.5	5.80	24.7	87.1	48.9	1.55	158	1.15	121	11.39

Notes.
[a] Regions are numbered according to the position (azimuthal) angles following the definition in T+21. The distance D is assumed to be ~3.5 kpc and ~3.7 kpc when the geometric and pressure center is used.
[b] Wind density profile is assumed to be $\rho(r) = ar^{-2}$, where $a = \dot{M}/(4\pi V_w)$ and wind velocity is fixed at $V_w = 250$ km s^{-1}.
[c] Best-fit radius of the outer boundary of the free-expanding wind.
[d] Average density gradient between the outer boundary of the free-expanding wind and the dense cloud.
[e] Radial separation of the FS in year 2015 from the cavity boundary.
[f] Density at $r = R_{2015}$.

6. Summary

Among Type Ia SNRs, Tycho has long been considered to be a prototypical remnant from the viewpoints of morphology, ambient environment, X-ray spectrum, and light echoes. However, recent radio and X-ray observations of Tycho (Katsuda et al. 2010; Williams et al. 2016) have shown azimuthal variability of the shock motion, and CO observations (Zhou et al. 2016) have suggested that Tycho is surrounded by a cloud with a cavity swept up by a past wind-like activity, which support the SD scenario. Moreover, reanalysis of Tycho's Chandra data has shown that since around 2007 Tycho's shock has been experiencing a substantial deceleration, which infers a recent interaction with a molecular cloud, supporting the picture of a cavity-wall environment. Such a nonuniform environment has strong implications on the nature of Tycho's progenitor system.

We have performed 1D hydrodynamic simulations to model the latest multiepoch proper motion measurements of Tycho's shock. We have tested two scenarios for the density structure in the cavity surrounded by a dense cloud, i.e., a uniform-density medium and a wind-like cavity. In the uniform-cavity case, all models fail to reproduce the large angular velocity in regions

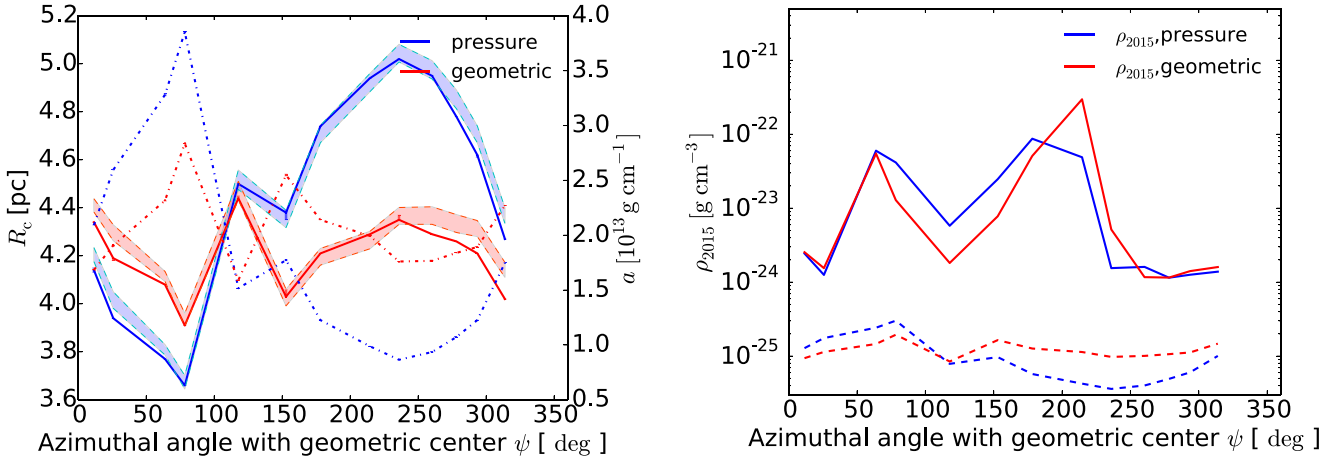

(a) Best-fit $a(\psi)$ and $R_c(\psi)$ (b) Best-fit $\rho(\psi)$

Figure 9. Best-fit output parameters as a function of azimuthal angle. Panel (a): the red solid line shows the cloud position R_c and the shaded band shows the radial range between the shock positions R_{2003} and R_{2015} in the 2003 and 2015 epochs, respectively, assuming the geometric explosion center. The blue line and shaded region are the counterparts assuming the pressure-gradient explosion center. The dashed–dotted lines indicate the corresponding best-fit wind parameter a. Panel (b): estimated gas densities vs. azimuthal angle. The solid lines show the estimated ambient gas density at the shock position in 2015. The dashed lines show the density at the position where the free-expanding wind ends (i.e., at the cavity's outer boundary).

like Regions 7 and 8 even by invoking an unrealistically low ambient density of 2.0×10^{-27} g cm^{-3}, leading us to consider a wind-like environment. In the wind-like cavity case, an anisotropic wind can provide a satisfactory fit to all regions. The best-fit parameter set in each region indicates a disk-like instead of a spherical isotropic mass-loss activity, with the wind density $a \sim 2 \times 10^{13}$ g cm^{-1} where $\rho(r) = ar^{-2}$. This can be converted to an estimate mass-loss rate $\sim 1 \times 10^{-5}\ M_\odot$ yr^{-1} for a wind velocity of 25 km s^{-1}, which may lead to the formation of a near-Chandrasekhar explosion. The total mass loss is estimated to be one to a few solar masses, which is within the scope of the SD scenario. Finally, our results have revealed an azimuthal variation of the cloud density, which can be explained by the clumpiness of the cloud.

Acknowledgments

We thank Professor Takashi Hosokawa at the Department of Physics of Kyoto University for a fruitful discussion on the parameters of the cloud. This work is supported by JSPS grant Nos. JP19K03913 (S.H.L.), JP19H01936 (T.T.), JP21H04493 (T.T.), and JP20H00174 (K.M.). R.K. acknowledges support by Science Faculty Scholarship from the Kyoto University Foundation, and JST, the establishment of university fellowships toward the creation of science technology innovation, grant No. JPMJFS2123. S.H.L. acknowledges support by the World Premier International Research Center Initiative (WPI), MEXT, Japan.

ORCID iDs

Ryosuke Kobashi https://orcid.org/0009-0008-4215-1049
Shiu-Hang Lee https://orcid.org/0000-0002-2899-4241
Takaaki Tanaka https://orcid.org/0000-0002-4383-0368
Keiichi Maeda https://orcid.org/0000-0003-2611-7269

References

Badenes, C., Borkowski, K. J., Hughes, J. P., Hwang, U., & Bravo, E. 2006, ApJ, 645, 1373
Blondin, J. M., & Ellison, D. C. 2001, ApJ, 560, 244
Chiotellis, A., Kosenko, D., Schure, K. M., Vink, J., & Kaastra, J. S. 2013, MNRAS, 435, 1659
Cui, Y., Meng, X., Podsiadlowski, P., & Song, R. 2022, A&A, 667, A154
Dwarkadas, V. V., & Chevalier, R. A. 1998, ApJ, 497, 807
Ferrand, G., Warren, D. C., Ono, M., et al. 2019, ApJ, 877, 136
Ghavamian, P., Rakowski, C. E., Hughes, J. P., & Williams, T. B. 2003, ApJ, 590, 833
Godinaud, L., Acero, F., Decourchelle, A., & Ballet, J. 2023, A&A, 680, A80
Guest, B. T., Borkowski, K. J., Ghavamian, P., et al. 2023, ApJ, 946, 44
Hachisu, I., Kato, M., & Nomoto, K. 1999, ApJ, 522, 487
Hayato, A., Yamaguchi, H., Tamagawa, T., et al. 2010, ApJ, 725, 894
Hwang, U., Decourchelle, A., Holt, S. S., & Petre, R. 2002, ApJ, 581, 1101
Jerkstrand, A., Maeda, K., & Kawabata, K. S. 2020, Sci, 367, 415
Kasuga, T. 2021, PhD thesis, Univ. Tokyo
Katsuda, S., Petre, R., Hughes, J. P., et al. 2010, ApJ, 709, 1387
Kerzendorf, W. E., Schmidt, B. P., Asplund, M., et al. 2009, ApJ, 701, 1665
Kobashi, R., Yasuda, H., & Lee, S.-H. 2022, ApJ, 936, 26
Kothes, R., Fedotov, K., Foster, T. J., & Uyanıker, B. 2006, A&A, 457, 1081
Krause, O., Tanaka, M., Usuda, T., et al. 2008, Natur, 456, 617
Lee, J.-J., Raymond, J. C., Park, S., et al. 2010, ApJL, 715, L146
Liu, Z. W., Pakmor, R., Röpke, F. K., et al. 2012, A&A, 548, A2
Livne, E. 1990, ApJL, 354, L53
Lopez, L. A., Grefenstette, B. W., Reynolds, S. P., et al. 2015, ApJ, 814, 132
Marietta, E., Burrows, A., & Fryxell, B. 2000, ApJS, 128, 615
Millard, M. J., Park, S., Sato, T., et al. 2022, ApJ, 937, 121
Meng, X., & Podsiadlowski, Ph. 2017, MNRAS, 469, 4763
Nomoto, K. 1982, ApJ, 253, 798
Nomoto, K. 1984, ApJ, 277, 791
Pakmor, R., Röpke, F. K., Weiss, A., & Hillebrandt, W. 2008, A&A, 489, 943
Pan, K.-C., Ricker, P. M., & Taam, R. E. 2012, ApJ, 750, 151
Perlmutter, S., Aldering, G., Goldhaber, G., et al. 1999, ApJ, 517, 565
Rappaport, S., Chiang, E., Kallman, T., & Malina, R. 1994, ApJ, 431, 237
Reynoso, E. M., Moffett, D. A., Goss, W. M., et al. 1997, ApJ, 491, 816
Riess, A. G., Filippenko, A. V., Challis, P., et al. 1998, AJ, 116, 1009
Ruiz-Lapuente, P., Comeron, F., Méndez, J., et al. 2004, Natur, 431, 1069
Sano, H., Yamaguchi, H., Aruga, M., et al. 2022, ApJ, 933, 157
Shen, K. J., & Bildsten, L. 2009, ApJ, 699, 1365
Slane, P., Lee, S.-H., Ellison, D. C., et al. 2014, ApJ, 783, 33
Soker, N. 2015, MNRAS, 450, 1333
Sparks, W. M., & Stecher, T. P. 1974, ApJ, 188, 149
Sutherland, R. S., & Dopita, M. A. 1993, ApJS, 88, 253
Tanaka, T., Okuno, T., Uchida, H., et al. 2021, ApJL, 906, L3
Warren, J. S., Hughes, J. P., Badenes, C., et al. 2005, ApJ, 634, 376
Williams, B. J., Borkowski, K. J., Ghavamian, P., et al. 2013, ApJ, 770, 129
Williams, B. J., Chomiuk, L., Hewitt, J. W., et al. 2016, ApJL, 823, L32
Woods, T. E., Ghavamian, P., Badenes, C., & Gilfanov, M. 2017, NatAs, 1, 800
Xue, Z., & Schaefer, B. E. 2015, ApJ, 809, 183
Yamaguchi, H., Eriksen, K. A., Badenes, C., et al. 2014, ApJ, 780, 136
Yamaguchi, H., Hughes, J. P., Badenes, C., et al. 2017, ApJ, 834, 124
Zhou, P., Chen, Y., Zhang, Z.-Y., et al. 2016, ApJ, 826, 34